ChemComm
Chemical Communications

Accepted Manuscript

This article can be cited before page numbers have been issued, to do this please use: Q. Zhao, K. Wang, X. Gao, H. Hsu and C. Tan, *Chem. Commun.*, 2026, DOI: 10.1039/D5CC05970D.

ROYAL SOCIETY OF CHEMISTRY

rsc.li/chemcomm

View Article Online
DOI: 10.1039/D5CC05970D

Journal Name

ARTICLE TYPE

Cite this: DOI: 00.0000/xxxxxxxxxx

Metal-Coordinated Porphyrin COFs Enable Efficient Visible-Light-Driven Photocatalytic NADH regeneration†

Qing-Ru Zhao,[a,†] Kui Wang,[b,†] Xiaokai Gao,[a] Hsien-Yi Hsu,*[,c] and Chunyan Tan*[,a,b]

Received Date
Accepted Date

DOI: 00.0000/xxxxxxxxxx

We present three porphyrin-based covalent organic frameworks (COFs), Por-BPy-COF1, Por-RhBPy-COF2, and ZnPor-RhBPy-COF3, synthesized as visible-light-responsive photocatalysts for NADH regeneration. These COFs incorporate porphyrin units that absorb visible light across a broad spectrum (200–680 nm), with Por-RhBPy-COF2 and ZnPor-RhBPy-COF3 further enhanced by rhodium and zinc metal coordination to promote charge separation. Notably, the rhodium-coordinated COFs (Por-RhBPy-COF2 and ZnPor-RhBPy-COF3) exhibited significantly higher catalytic activity ($\sim 41-46\%$ in 1 hour) compared to Por-BPy-COF1 (2.6%), attributed to rhodium's bioinspired role in facilitating NAD^+ reduction. Structural stability and sustained catalytic performance were confirmed, with Por-RhBPy-COF2 maintaining $> 37\%$ activity during a 1-hour cyclic NADH regeneration test. These findings highlight the potential of these COFs for efficient solar-to-chemical energy conversion, advancing sustainable photocatalytic technologies.

Natural photosynthesis inspires sustainable solar-to-chemical conversion, utilizing chlorophyll-based light harvesting and biosynthetic specificity.[1] This has led to artificial photosynthesis, which employs semiconductor photocatalysts to generate charge carriers for fuel synthesis.[2–4] However, such systems suffer from poor selectivity and limited capacity to form complex multi-carbon compounds, underscoring the need for materials that combine artificial efficiency with natural precision.[5,6]

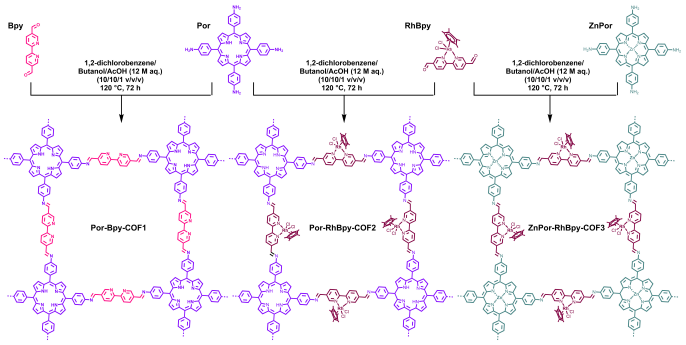

Scheme 1 Synthesis of Por-Bpy-COF1, Por-RhBpy-COF2, and ZnPor-RhBPy-COF3.

Semi-artificial photosynthesis combines artificial light harvesters with biological catalysts, improving solar energy utilization and high-value chemical production while overcoming the limitations of purely natural or artificial systems.[7–12] Coenzymes such as reduced nicotinamide adenine dinucleotide (NADH) are essential biological cofactors that mediate redox reactions and act as "energy currency" in living systems. Photocatalytic NADH regeneration is therefore crucial for advancing enzyme-coupled and whole-cell systems, underpinning the development of complex semi-artificial photosynthetic applications.[13–15]

Covalent organic frameworks (COFs) are promising candidates due to their tunable structures, photoactivity, stability, and porosity.[16,17] Porphyrins serve as efficient visible-light chromophores with rapid electron transfer, while their porous, rigid frameworks enable recyclability after metal coordination and repeated use.[18–20] Porphyrin-based COFs, incorporating nature-inspired porphyrins for visible light absorption, excel in light harvesting, biocompatibility, and charge transport.[21,22] Metal coordination (e.g., Rh, Zn) further enhances COFs by aligning charge carrier levels with target reactions, acting as catalytic sites, and promoting enzyme interactions.[23] Additionally, metal centers act as catalytic sites, improve structural rigidity, and promote interactions

[a]Institute of Biopharmaceutical and Health Engineering, Tsinghua Shenzhen International Graduate School, Tsinghua University, Shenzhen 518055, P. R. China. E-mail: tancy@sz.tsinghua.edu.cn
[b]Open FIESTA, Tsinghua Shenzhen International Graduate School, Tsinghua University, Shenzhen 518055, P. R. China
[c]Department of Materials Science and Engineering, School of Energy and Environment, City University of Hong Kong, Kowloon Tong, Hong Kong, China. E-mail: sam.hyhsu@cityu.edu.hk
†These authors contributed equally to this work.

† Supplementary Information available: [details of any supplementary information available should be included here]. See DOI: 00.0000/00000000.

View Article Online
DOI: 10.1039/D5CC05970D

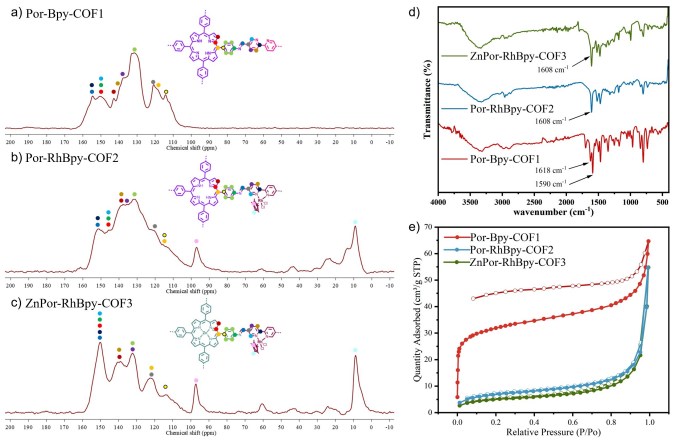

Fig. 1 (a–c) Solid-state ^{13}C CP/MAS NMR spectra, (d) Fourier transform infrared (FTIR) spectra, and (e) nitrogen adsorption isotherms of Por-Bpy-COF1, Por-RhBpy-COF2, and ZnPor-RhBPy-COF3.

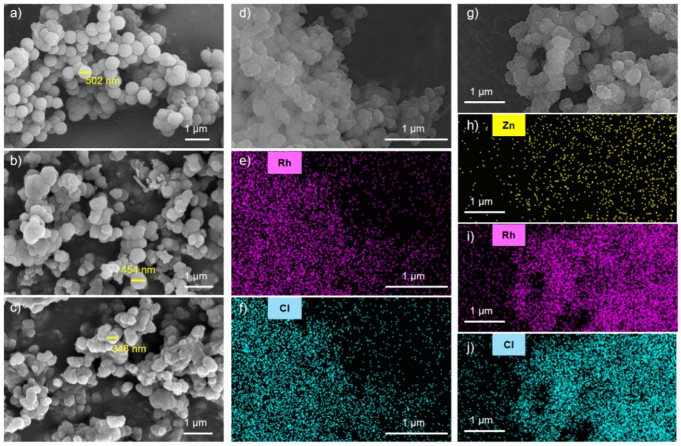

Fig. 2 (a–c) Scanning electron microscopy (SEM) images of Por-Bpy-COF1, Por-RhBpy-COF2, and ZnPor-RhBPy-COF3. (d–f) Energy-dispersive X-ray spectroscopy (EDS) mapping images of Por-RhBpy-COF2. (g–j) EDS mapping images of ZnPor-RhBPy-COF3.

with enzymes.[24] Despite their potential, metal-coordinated porphyrin COFs remain underexplored in enzyme-integrated semi-artificial photosynthesis, particularly for photocatalytic NADH regeneration, with current strategies relying on less stable and less biocompatible inorganic semiconductors and organic photosensitizers.[25,26]

Herein, we address this gap by developing three recyclable 2D porphyrin-based COFs (Por-Bpy-COF1, Por-RhBPy-COF2, ZnPor-RhBPy-COF3, Scheme 1) for efficient visible-light-driven photocatalytic NADH regeneration.

We employed multiple characterization techniques to confirm the synthesis of the three catalysts. The structural integrity of these catalysts was verified through solid-state ^{13}C cross-polarized magic-angle spinning (CP/MAS) nuclear magnetic resonance spectroscopy and Fourier transform infrared (FTIR) spectroscopy.The successful synthesis of Por-Bpy-COF1, Por-RhBpy-COF2, and ZnPor-RhBPy-COF3 was verified via solid-state ^{13}C cross-polarization magic-angle spinning (CP/MAS) NMR spectroscopy (Fig. 1a–c). The presence of an imine carbon resonance peak at 150 ppm and the absence of residual aldehyde signals ($\sim$ 190 ppm) confirmed the full condensation of the monomers. Aromatic carbon signals (120–140 ppm) corresponding to porphyrin and bispyridine units remained intact across all three COFs, verifying framework structural preservation during synthesis. Notably, the deshielded peak at 150 ppm was significantly enhanced in Por-RhBpy-COF2 and ZnPor-RhBPy-COF3, an effect attributed to rhodium- and zinc-induced electron density redistribution on the coordinated pyridine carbons. Concurrently, a peak associated with the methylcyclopentane group appeared near 10 ppm, further confirming the target framework composition.

Fourier transform infrared (FTIR) spectroscopy further validated imine bond formation in all three COFs (Fig. 1d). Characteristic C=N stretching vibration peaks were observed at 1590 cm^{-1} for Por-Bpy-COF1 and 1607 cm^{-1} for both Por-RhBpy-COF2 and ZnPor-RhBPy-COF3, with minimal shifts between samples. This subtle spectral variation indicates that Rh and Zn coordination exerted a negligible influence on the electronic environment of imine bonds, supporting COF backbone structural integrity post-metallation.

Nitrogen adsorption measurements at 77 K revealed distinct differences in the pore structures of the three COFs (Fig. 1e). The Brunauer–Emmett–Teller (BET) surface area of Por-Bpy-COF1 (118 m^2/g) was markedly higher than those of Por-RhBpy-COF2 (25 m^2/g) and ZnPor-RhBPy-COF3 (18 m^2/g). Functionalization of COFs alters their pore volume and surface area, as functional groups or metal complexes occupy pore space and affect interlayer interactions.[27,28] Metallized COFs (Por-RhBpy-COF2 and ZnPor-RhBPy-COF3) exhibit reduced BET surface area due to (1) bulkier Rh complexes occupying internal voids and (2) enhanced interlayer dispersion forces from Rh coordination, which mitigates full pore collapse. BET isotherms (Fig. 1e) corroborate this, with all samples retaining a mesoporous structure (2–5 nm; Fig. S1). This preserved mesoporosity boosts substrate accessibility and charge localization without sacrificing photocatalytic performance. By improving mass transport and suppressing hole recombination, the architecture offers vital advantages for efficient photochemical energy conversion and biophotocatalysis.[29–32]

SEM images showed that Por-Bpy-COF1, Por-RhBpy-COF2, and ZnPor-RhBPy-COF3 all self-assembled into spherical aggregates with diameters of 340–500 nm (Fig. 2a–c), a morphology indicative of isotropic growth under kinetic control. Energy-dispersive X-ray spectroscopy (EDS) was used to confirm elemental composition and spatial distribution. For Por-RhBpy-COF2, EDS mapping (Fig. 2d–f) revealed highly uniform overlap between COF framework, Rh, and Cl signals. For ZnPor-RhBPy-COF3, EDS mapping (Fig. 2g–j) similarly showed uniform distribution of Zn, Rh, and Cl across COF aggregates, confirming successful incorporation and homogeneous dispersion of both metal coordination groups throughout the framework.

To elucidate the COFs' photocatalytic mechanism, their photophysical properties were systematically characterized. Ultraviolet–visible diffuse reflectance spectroscopy (UV-DRS) analysis revealed broad absorption bands spanning 200–680 nm for all three COFs (Fig. 3a). This broad absorption is attributed to the

View Article Online
DOI: 10.1039/D5CC05970D

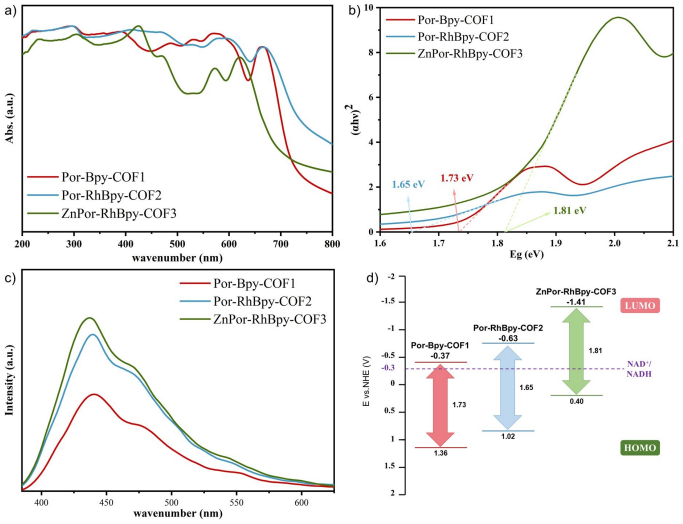

Fig. 3 (a) UV-DRS spectra, (b) Tauc plots for bandgap calculation, (c) steady-state photoluminescence (PL) spectra, and (d) band structures of Por-Bpy-COF1, Por-RhBpy-COF2, and ZnPor-RhBPy-COF3.

intrinsic optical properties of porphyrins and π-π stacking interactions within COF frameworks, which collectively enhance light absorption. Tauc plots, derived from Kubelka–Munk transformation, indicated optical bandgaps of 1.73 eV (Por-Bpy-COF1), 1.65 eV (Por-RhBpy-COF2), and 1.81 eV (ZnPor-RhBPy-COF3; Fig. 3b). These narrow bandgaps make the COFs highly suitable for biophotocatalytic applications, as they facilitate efficient visible-light harvesting. Fluorescence measurements (365 nm excitation; Fig. 3c) revealed photoluminescence (PL) peaks centered near 450 nm for all three COFs, with a slight blue shift observed for metallated COFs (Por-RhBpy-COF2 and ZnPor-RhBPy-COF3). The PL peak positions—shaped by contributions from multiple excited states rather than solely the HOMO–LUMO energy gap—were nearly identical across the three COFs, confirming similar bandgap widths and consistent with Tauc plot results.

X-ray photoelectron spectroscopy (XPS) valence band spectra confirmed n-type semiconductor behavior for all three COFs, as indicated by their negative tangent slopes. The highest occupied molecular orbital (HOMO) levels, referenced to the normal hydrogen electrode (NHE), were measured as 1.36 V (Por-Bpy-COF1), 1.02 V (Por-RhBpy-COF2), and 0.40 V (ZnPor-RhBPy-COF3; Fig. S2). Using these HOMO values and corresponding bandgaps, the lowest unoccupied molecular orbital (LUMO) energies were calculated via the relationship $E_{\mathrm{LUMO}} = E_{\mathrm{HOMO}} + E_g$. This analysis yielded LUMO potentials of -0.37 V (Por-Bpy-COF1), -0.63 V (Por-RhBpy-COF2), and -1.41 V (ZnPor-RhBPy-COF3). These values provide sufficient thermodynamic driving force for single-electron oxygen reduction, as depicted in the band structure (Fig. 3d).

Electrochemical characterization revealed distinct charge-transfer behavior for metallated COFs. Transient photocurrent measurements (Fig. S3) showed that Por-RhBpy-COF2 and ZnPor-RhBPy-COF3 exhibit higher current densities than Por-Bpy-COF1, while electrochemical impedance spectroscopy (EIS; Fig. S4) indicated smaller semicircular radii for metallated samples. Both observations are indicative of lower charge-transfer resistance. Notably, the coenzyme regeneration system, central to semi-artificial photosynthesis, relies on NADH as the primary target, where regeneration is achieved through the synergistic interaction of photocatalysts, electron donors, and electron mediators. Collectively, these results confirm that all three COFs exhibit strong visible-light absorption, band structures compatible with photocatalytic applications (including coverage of the NADH reduction potential), and enhanced photoelectrochemical performance upon metal coordination, laying the experimental groundwork for their use in biophotocatalytic NADH regeneration.

Key parameters for photocatalytic NADH regeneration—such as pH, light source, and comparisons with non-porphyrin COFs—were first optimized (Figs. S5–S9). Under the optimized condition, the NADH regeneration performance of the three target COFs (Por-BPy-COF1, Por-RhBPy-COF2, ZnPor-RhBPy-COF3) was systematically evaluated using a 350 W xenon lamp.

We propose a detailed electron transfer mechanism (Fig. 4a). Upon visible light irradiation, the porphyrin unit in Por-RhBpy-COF2 absorbs photons, generating separated electron-hole pairs (h^+/e^-). The Rh center in the COF acts as a biomimetic electron mediator, mimicking the function of natural metalloenzymes to facilitate efficient electron transfer for NADH regeneration.

Figure 4b compares the photocatalytic NADH regeneration activities of the three COFs. Metal-free Por-BPy-COF1 shows the lowest activity ($\sim$ 10%) due to poor charge separation. Por-RhBPy-COF2 exhibits moderate activity ($\sim$ 30%), enhanced by Rh-mediated electron transfer. ZnPor-RhBPy-COF3 achieves the highest activity ($\sim$ 42%), attributed to metal synergy and the biomimetic Rh complex acting as an efficient electron mediator for selective 1,4-NADH regeneration. Time-dependent experiments revealed distinct kinetic behaviors. Por-BPy-COF1 exhibited a steady increase in regeneration rates over 0–6 hours, peaking at $\sim$ 20% at 6 hours. In contrast, Por-RhBPy-COF2 and ZnPor-RhBPy-COF3 showed rapid rate increases over 0–2 hours, maintaining levels above 60% with minor fluctuations between 4–6 hours. The maximum regeneration rates of Por-RhBPy-COF2 and ZnPor-RhBPy-COF3 were over three times higher than that of Por-BPy-COF1, further confirming Rh's specific catalytic role. The comparable performance of Por-RhBPy-COF2 and ZnPor-RhBPy-COF3, with Por-RhBPy-COF2 showing a slight advantage, suggests that Zn coordination has a negligible impact on efficiency. This is likely because theoretical light absorption enhancements from Zn are offset by reduced COF molar concentration, as Zn occupies mass without increasing active sites.

Non-porphyrin Rh-COFs (ETTA-RhBpy-COF, TAPB-RhBpy-COF; Fig. S8–S9) showed significantly lower 1-h regeneration rates (7.88% and 3.92%, respectively) than Por-RhBpy-COF2. This difference arises because (1) their lack of porphyrin units limits visible-light absorption, evident from their lighter color compared to the deep black porphyrin-based COFs, and (2) their band structures do not span the -0.3 V reduction potential required for NADH regeneration. These results underscore the unique advantage of porphyrin-based COFs and the importance of monomer selection in COF design. Increasing the catalyst from 1 to 4 mg moderately raised the NADH yield from 35% to 41% (Fig. S10).

View Article Online
DOI: 10.1039/D5CC05970D

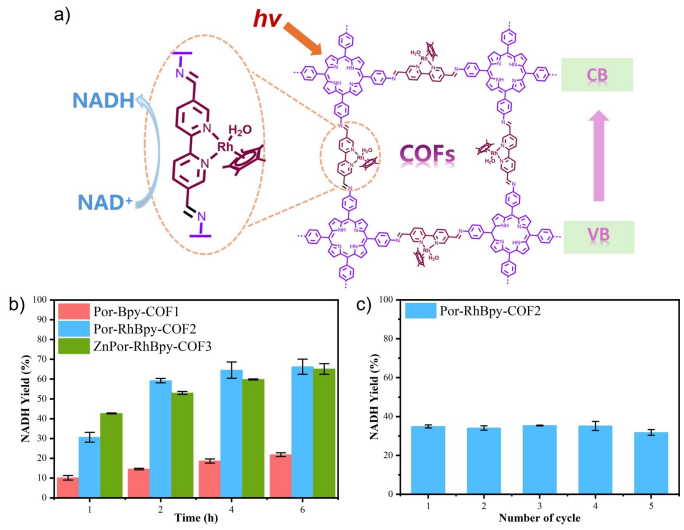

Fig. 4 (a) Schematic of the photocatalytic NADH regeneration system, (b) NADH regeneration rates of the three COFs after different periods of time (1-6 h), and (c) recyclability of Por-RhBpy-COF2 over five cycles.

To evaluate the practical utility of the COFs, we assessed the recyclability of Por-RhBpy-COF2 (Fig. 4c). After each 1-hour photocatalytic cycle, the solid COF was recovered through centrifugation and reused. Over five consecutive cycles, the catalytic efficiency remained stable at approximately 37%, with no significant degradation. This exceptional stability is further supported by the absence of dissolution or decomposition of Por-RhBpy-COF2 in aqueous dispersion under continuous irradiation. Notably, light absorption, electron–hole separation, and Rh active-site activity were unaffected, underscoring the unique advantage of COFs as recyclable biophotocatalysts. Following catalyst recovery and recharacterization, solid-state NMR (Fig. S11) and infrared spectroscopy (Fig. S12) revealed that the regenerated catalyst was identical to the initial catalyst, demonstrating exceptional chemical stability and photostability.

In conclusion, we designed and synthesized three recyclable 2D porphyrin-based COFs (Por-Bpy-COF1, Por-RhBpy-COF2, ZnPor-RhBPy-COF3) for visible-light-driven NADH regeneration. Their structural integrity, broad visible absorption (200–680 nm), and suitable band positions jointly enable efficient photocatalysis: metallated COFs (ZnPor-RhBPy-COF3: 42%; Por-RhBpy-COF2: 30% regeneration rate at 1 h) outperform the metal-free Por-Bpy-COF1 (10%) by over threefold, attributed to Rh acting as biomimetic sites for selective electron transfer to NAD^+. Por-RhBpy-COF2 retains 37% activity over five cycles, confirming stability. Comparisons with non-porphyrin Rh-COFs underscore the essential role of porphyrin units in meeting the NADH reduction potential. This work provides efficient, reusable porphyrin-COFs for NADH regeneration and demonstrates a rational metal-coordination design strategy, advancing COFs toward semi-artificial photosynthesis and enzyme-integrated synthesis.

This work is supported by the State Key Laboratory of Chemical Oncogenomics, and the Basic and Applied Basic Research Foundation of Guangdong Province (2025A1515011980).

Conflicts of interest

There are no conflicts to declare.

Data availability

The data supporting this article have been included as part of the Supplementary Information. Supplementary information: characterization results in Figures S1-12, and further experimental details. See DOI: https://doi.org/DOI†

Notes and references

1 N. Nelson and A. Ben-Shem, *Nat. Rev. Mol. Cell Biol.*, 2004, **5**, 971–982.
2 X. Fang, S. Kalathil and E. Reisner, *Chem. Soc. Rev.*, 2020, **49**, 4926–4952.
3 X.-G. Zhu, S. P. Long and D. R. Ort, *Annu. Rev. Plant Biol.*, 2010, **61**, 235–261.
4 R. E. Blankenship, D. M. Tiede, J. Barber *et al.*, *Science*, 2011, **332**, 805–809.
5 S. Cestellos-Blanco, H. Zhang and P. Yang, *Faraday Discuss.*, 2019, **215**, 54–65.
6 J. Jia, L. C. Seitz, J. D. Benck *et al.*, *Nat. Commun.*, 2016, **7**, 13237.
7 K. K. Sakimoto, A. B. Wong and P. Yang, *Science*, 2016, **351**, 74–77.
8 H. Zhang, H. Liu, Z. Tian *et al.*, *Nat. Nanotechnol.*, 2018, **13**, 900–905.
9 K. A. Brown, M. B. Wilker, M. Boehm *et al.*, *ACS Catal.*, 2016, **6**, 2201–2204.
10 T. W. Woolerton, S. Sheard, E. Reisner *et al.*, *J. Am. Chem. Soc.*, 2010, **132**, 2132–2133.
11 B. Luo, Y.-Z. Wang, D. Li *et al.*, *Adv. Energy Mater.*, 2021, **11**, 2100256.
12 P. Gai, W. Yu, H. Zhao *et al.*, *Angew. Chem. Int. Edit.*, 2020, **59**, 7224–7229.
13 N. Kornienko, J. Z. Zhang, K. K. Sakimoto *et al.*, *Nat. Nanotechnol.*, 2018, **13**, 890–899.
14 Y. Peng, Z. Chen, J. Xu *et al.*, *Org. Process Res. Dev.*, 2022, **26**, 1900–1913.
15 M. A. Emmanuel, S. G. Bender, C. Bilodeau *et al.*, *Chem. Rev.*, 2023, **123**, 5459–5520.
16 P. J. Waller, F. Gandara and O. M. Yaghi, *Accounts Chem. Res.*, 2015, **48**, 3053–3063.
17 S. Chandra, D. R. Chowdhury, M. Addicoat *et al.*, *Chem. Mat.*, 2017, **29**, 2074–2080.
18 P. Asselin and P. D. Harvey, *ACS Appl. Nano Mater.*, 2022, **5**, 6055–6082.
19 X. Liu, R. Qi, S. Li *et al.*, *J. Am. Chem. Soc.*, 2022, **144**, 23396–23404.
20 Y. Bai, W. Gao, J. Wei *et al.*, *Chem. Eng. J.*, 2024, **490**, 151628.
21 J. Chen, S. Yan, F. Wang *et al.*, *Angew. Chem. Int. Edit.*, 2025.
22 D. Yadav, A. Kumar, J. Y. Kim *et al.*, *J. Mater. Chem. A*, 2021, **9**, 9573–9580.
23 S. H. Lee, D. S. Choi, S. K. Kuk *et al.*, *Angew. Chem. Int. Edit.*,

View Article Online
DOI: 10.1039/D5CC05970D

2018, **57**, 7958–7985.
24 D. Monti, G. Ottolina, G. Carrea *et al.*, *Chem. Rev.*, 2011, **111**, 4111–4140.
25 G. Lin, Y. Zhang and J. Liu, *Prog. Chem.*, 2022, **34**, 2351–2360.
26 X. Wu, S. Wang, J. Fang *et al.*, *ACS Appl. Mater. Interfaces*, 2022, **14**, 38895–38904.
27 A. Nagai, Z. Guo, X. Feng *et al.*, *Nat. Commun.*, 2011, **2**, 536.
28 D. Zhu, J.-J. Zhang, X. Wu *et al.*, *Chem. Sci.*, 2022, **13**, 9655–9667.
29 W. Che, S. Zhao, W. J. Byun *et al.*, *Adv. Mater.*, 2025, **37**, e06961.
30 J. Tang, Y. Lei, Q. Tang *et al.*, *Angew. Chem. Int. Edit.*, 2025, e202516599.
31 L. Tong, Z. Gong, Y. Wang *et al.*, *J. Am. Chem. Soc.*, 2024, **146**, 21025–21033.
32 H. Zheng, Z. Huang, P. Wei *et al.*, *ACS Sustain. Chem. Eng.*, 2025, **13**, 4078–4092.

View Article Online
DOI: 10.1039/D5CC05970D

Data availability

The data supporting this article have been included as part of the

Supplementary Information. Supplementary information: characterization results in Figures S1-12, and further experimental

details. See DOI: https://doi.org/DOI†